Quantification of Hysteresis and Nonlinear Effects on the Frequency Response of Ferroelectric and Ferromagnetic Materials

M Stuebner[1], J Atulasimha[2] and R C Smith[1]

[1] Department of Mathematics and Center for Research in Scientific Computation, North Carolina State University, Raleigh, NC 27695-8205

[2]Department of Mechanical Engineering, Virginia Commonwealth University, Richmond, VA 23284-3015

E-mail: `mstuebn@ncsu.edu`

Abstract. Ferroelectric (e.g., PZT and PMN) and ferromaqnetic (e.g., Terfenol-D) materials exhibit high energy densities, broadband drive capabilities, and the capacity for both actuating and sensing. This makes them attractive as compact transducers for applications including nanopositioning systems such as atomic force microscopes (AFM), acoustic transducers, and drive mechanisms for high speed milling. However, these materials also exhibit hysteresis and constitutive nonlinearities at all drive levels. To achieve stringent tracking requirements, it is critical to understand and quantify the effect of hysteresis and nonlinearities on the frequency behavior of devices that employ these compounds. Whereas considerable progress has been made on model development and understanding these materials in the parameter space and time domain, comprehensive quantification of these effects in the frequency domain is presently lacking. In this paper, we investigate both numerically and experimentally the effect of hystersis, constitutive nonlinearities, bias fields and AC drive levels on the frequency domain behavior of ferroelectric and ferromagnetic materials.

1. Introduction

Ferromagnetic and ferroelectric materials are increasingly considered for use as actuators and sensors due to their broadband drive capabilites and their relatively high energy densities. Ferromagnetic materials such as Terfenol-D are being investigated for use in high speed milling devices, sonar transducers, vibration attentuation devices and ultrasonic transducers [8, 9, 18]. Ferroelectric materials such as PZT are presently employed in essentially all nanoposition systems such as atomic force microscopes (AFM) due to their high set point accuracy [20]. As detailed in [25], this property also makes them advantageous for use in the focusing mechanisms for miniature cameras and ultrasonic motors. Additionally, PZT-based transducers are being investigated for vibration attenuation and noise control whereas PMN is is considered for sonar transduction [19].

However, the advantages provided by ferroelectric and ferromagnetic compounds come at the cost of hysteresis and constitutive nonlinearities at all drive levels. For certain applications, one can minimize these deletarious effects by operating the actuators in near-linear regimes by allowing only small perturbations about bias input fields. However, this limits the degree to which the large force capabilities of the devices can be utilized for high performance applications. Alternatively, charge or current controlled amplifiers can minimize observed hysteresis in ferroelectric actuators [15, 16]. However, charge control is ineffective if constant positions must be maintained (e.g., holding the x-stage in an AFM constant while a sweep is made in y) and these amplifiers are often significantly more expensive than traditional voltage-control devices.

An increasingly attractive alternative is to employ comprehensive constitutive models to construct inverse compensators that approximately linearize the hysteresis [4, 13, 22, 23, 24]. This permits the implementation of linear control algorithms while operating the devices in highly nonlinear and hysteretic regimes. It should be noted, however, that these inverse models are necessarily approximations of the physical behavior and the accuracy of this approximation typically degrades as operating regimes become increasingly complex due to temperature, frequency, and stress effects as well as changing bias levels.

Quantification of the effects of hysteresis and nonlinearities on the frequency behavior of systems employing ferroelectric and ferromagnetic materials is important from both fundamental and technological perspectives. From a fundamental perspective, it provides a means of understanding the manner through which higher harmonics and other nonlinear effects are produced by the materials. From the perspective of inverse compensator-based control design, such analysis is necessary to quantify the effects of approximate inversion and determine the degree to which robust control design must attenuate undesirable frequencies while achieving tracking specifications.

A limited analysis of the frequency response of hysteretic systems has been reported in literature. Frequency responses of single degree of freedom hysteretic systems have been studied by Christopoulos [7] while oscillations of a hysteretic two degree of freedom

system are reported in by [6]. Zhang [26] had developed an innovative tool to visualize the spectral structure of the hysteretic nonlinear system. By plotting the gain as a function of input and output frequencies using a three-dimensional plot, cross gain transfer functions between various frequencies can be easily understood. However, the models used for the hysteretic systems in these papers are not representative of general ferromagnetic and ferroelectric behavior. Hence, the methods existing in literature are still limited with regard to providing a comprehensive understanding and quantification regarding the frequency response of ferroelectric and ferromagnetic materials.

In this paper, we investigate the effects of hysteresis, nonlinearities, bias fields and AC drive levels on the frequency domain behavior of ferroelectric and ferromagnetic materials using the Homogenized Energy Model (HEM). This model incorporates thermal relaxation, rate effects, material non-homogeneities, polycrystallinity, etc and exhibits minor loop closure in the absence of relaxation making it a good tool to understanding the dynamics of and controlling ferroelectric and ferromagnetic materials [21]. To provide context we first briefly compare this framework with others commonly used to characterize hysteresis.

The Jiles-Atherton model [14] models ferromagnetic behavior as comprised of domain rotation and domain wall pinning. A modified Langevin equation is employed to model the bulk anhysteretic magnetization (magnetization field curve without hysteresis). The motion of domain walls is modeled as impeded by the presence of pinning sites leading to hysteresis. A shortcoming of this model is that some artificial conditions have to be applied to ensure minor loop closure.

The Armstrong model was constructed to include the magnetocrystalline, magneto-elastic and magnetic field energy terms. For a given value of applied stress and magnetic field in any direction, the total energy (sum of the three above mentioned energy terms) corresponding to the magnetization vector being oriented along different directions is evaluated [1]. The probability that the magnetization takes a particular orientation depends on the total energy corresponding to that orientation; the lower this energy the greater the probability that this state is occupied. By performing a probability weighted summation over all the states, the average macroscopic property of this material was evaluated. A hysteretic version was developed later [2] and extended to model hysteresis in multiple crystallographic directions [3]. While these models are capable of comprehensively modeling three-dimensional quasi-static behavior and exhibit minor loop closure, they are incapable of modeling certain experimentally observed trends in minor loops.

Preisach models have been widely employed to characterize hysteresis and non-linearities in both ferromagnetic and ferroelectric materials [19]. As detailed in [17], classical Preisach models are characterized by the conditions of congruency and deletion. To accommodate stress and rate-dependent effects, a number of generalized Preisach models have been proposed for both classes of compounds [10]. Whereas these generalized models models extend the applicability of the framework, they come at a significant loss in efficiency which presently prohibits real-time implementation for

high frequency applications.

The Homogenized Energy Model [21] was chosen to study the dynamic behavior of ferroelectric and ferromagnetic materials due to its capability for characterizing a range of minor loop behavior under highly varied operating conditions. Extensions to the orignal framework include the incorporation of magnetocrystalline and magneto-elastic terms [12]. However, we focus on the original formulation of the Homogenized Energy Model [21] since it sufficiently quantifies the dynamic behavior of ferroelectric and ferromagnetic materials under the considered operating conditions.

A short description of the Homogenized Energy Model and its use to construct a discretized PDE model for a vibrating beam is provided in Sections 2 and 3. This is followed by numerical simulations of the behavior of Terfenol-D [11] and PZT5H [19] using model parameters identified from experimental data. This illustrates the dynamic behavior of the materials in time, frequency and parameter space. In the Section 5, the beam model with polarization quantified by the Homogenized Energy Model is compared with experimental beam data exhibiting both the driving frequency and higher harmonics induced by the hysteresis and constitutive nonlinearities. It is illustrated that the dynamic model accurately quantifies these effects in the phase space as well as time and frequency domains.

2. Homogenized Energy Model

The homogenized energy model for ferroelectric and ferromagnetic materials is a multi-scale approach based on energy relations and stochastic homogenization techniques. For ferroelectric materials the macroscopic model quantifies the bulk polarization P by

$$[P(E)](t) = \int_0^\infty \int_{-\infty}^\infty \nu_1(E_c)\nu_2(E_I)[\bar{P}(E + E_I; E_c, \xi)](t)\, dE_I\, dE_c \tag{1}$$

where E is the applied electric field, E_I is the field due to dipole interactions, E_c is the coercive field value at which the dipoles switch orientation, and ξ denotes the initial distribution of dipoles. For ferromagnetic materials the analogous model for the bulk magnetization M is given by

$$[M(H)](t) = \int_0^\infty \int_{-\infty}^\infty \nu_1(H_c)\nu_2(H_I)[\bar{M}(H + H_I; H_c, \xi)](t)\, dH_I\, dH_c \tag{2}$$

where H is the magnetic field. The model parameters E_c/H_c and E_I/H_I vary through the material and have associated densities ν_1 and ν_2. Throughout this section the equations are given in terms of polarization and electric field.

The integrals in (1) are numerically approximated using quadrature formulas to yield the discrete relation

$$[P(E)](t) = \sum_{i=1}^{N_i} \sum_{j=1}^{N_j} \nu_1(E_c)\nu_2(E_I)[\bar{P}(E + E_I; E_c, \xi)](t) v_i w_j \tag{3}$$

where E_{I_j}, E_{c_i} denote the points associated with the quadrature formulas and v_i, w_j are the quadrature weights.

For the density of the coercive field, one could choose a lognormal distribution

$$\nu_1(E_c) = \frac{1}{s\sqrt{2\pi}E_c} \exp\left(-\frac{\ln E_c - m}{2s}\right)^2 \tag{4}$$

where s and m are given in terms of standard deviation c and mean $\bar{E}_c$

$$s = \sqrt{\ln\left(1 + \frac{c^2}{\bar{E}_c^2}\right)} \tag{5}$$

$$m = \ln \bar{E}_c - \frac{1}{2}\ln\left(1 + \frac{c^2}{\bar{E}_c^2}\right). \tag{6}$$

Another choice could be

$$\nu_1(E_c) = c_1 \exp\left(-\frac{\ln E_c - \ln \bar{E}_c}{2s}\right)^2 \tag{7}$$

with

$$c_1 = \left(\int_0^\infty \exp\left(-\frac{\ln E_c - \ln \bar{E}_c}{2s}\right)^2 dE_c\right)^{-1}. \tag{8}$$

A choice for the distribution of the density of the interaction field is the Gaussian relation

$$\nu_2(E_i) = \frac{1}{s\sqrt{2\pi}} \exp\left(-\frac{E_i}{2b}\right)^2. \tag{9}$$

More general choices for the densities can be found in [19].

The kernel $\bar{P}$ is modeled via energy principles. For neglegible thermal relaxation direct minimization of the Gibbs energy yields the kernel $\bar{P}$

$$\bar{P}(E) = \frac{1}{\eta}E + P_R\delta(E; E_c, E_I), \tag{10}$$

where P_R is the remanence polarization and $\delta = 1$ if dipoles are positively oriented and $\delta = -1$ if they are negative. It should be noted that δ represents the history of the material and is remembered from the previous condition.

If thermal relaxation mechanisms are considered, one has to include the effects of thermal activation. This can be done by balancing the Gibbs energy with the relative thermal energy through the Boltzmann relation

$$\mu(G) = C \exp\left(-\frac{GV}{kT}\right) \tag{11}$$

where k is Boltzmann's constant, T is the temperature of the material and V is a reference volume. The resulting kernel is then given by

$$\bar{P} = x_+\langle P_+\rangle + x_-\langle P_-\rangle. \tag{12}$$

The evolution of dipole fractions is quantified by the differential equations

$$\dot{x}_+ = -p_{+-}x_+ + p_{-+}x_- \tag{13}$$

$$\dot{x}_- = -p_{-+}x_- + p_{+-}x_+ \tag{14}$$

where $\langle P_+ \rangle$ and $\langle P_- \rangle$ are the expected polarizations and p_{+-} and p_{-+} the transition likelihoods which include the material and temperature dependent relaxation time τ. These quantities can be expressed in terms of error functions. For detailed expressions and implementation of the thermally relaxed model see [4].

For neglegible relaxation the model is characterized by the five parameters η, $\bar{E}_c/\bar{M}_c$, P_r/M_r, c and b. If thermal relaxtion is included there are the additional two parameters τ and $\gamma = \frac{V}{kT}$.

3. Beam Model

The relation (1) quantifies the polarization P as a function of the input field E. In this section, we summarize how this can be used to develop a dynamic model of an Euler-Bernoulli beam driven by surface mounted piezoceramic patches. Analogous analysis can be used to incorporate the inputs due to magnetic transducers.

Motivated by the experimental setup stated in Section 5, we consider a thin cantilever beam of length ℓ, width b and thickness h that is clamped at $x = 0$ and free at $x = \ell$. We let ρ, YI, cI and γ respectively denote the effective linear density, stiffness, Kelvin-Voigt damping and air damping coeficients and we let $w(t, x)$ denote the transverse displacement of the beam. The mass of a surface-mounted accelerometer at $x = \bar{x}$ is denoted by m_{acc} and the region covered by the patches is designated by $[x_1, x_2]$. The following model is detailed in Chapter 7 of [19].

Force and moment balancing yield the strong model formulation

$$\begin{aligned} &\rho\frac{\partial^2 w}{\partial t^2} + \gamma\frac{\partial w}{\partial t} - \frac{\partial^2 M}{\partial x^2} = 0 \\ &w(t,0) = \frac{\partial w}{\partial x}(t,0) = 0 \\ &M(t,\ell) = \frac{\partial M}{\partial x}(t,\ell) = 0 \\ &w(0,x) = w_0(x) \quad , \quad \frac{\partial w}{\partial t}(0,x) = w_1(x) \end{aligned} \tag{15}$$

where the moment is

$$M(t,x) = -YI\frac{\partial^2 w}{dx^2} - cI\frac{\partial^3 w}{dx^2 \partial t} + k_1[P(E(t)) - P_R]\chi_{pe}(x)$$

and ρ incorporates the accelerometer mass m_{acc}. Here P is quantified by (1) and the characteristic function

$$\chi_{pe}(x) = \begin{cases} 1 & , \quad x \in [x_1, x_2] \\ 0 & , \quad x \in [0, x_1) \cup (x_2, \ell], \end{cases}$$

isolates inputs to the region covered by the patches.

To faciliate analysis and numerical implementation, we employ the resulting weak formulation

$$\begin{aligned}\int_0^\ell \rho\frac{\partial^2 w}{\partial t^2}\phi\,dx + \int_0^\ell \gamma\frac{\partial w}{\partial t}\phi\,dx + \int_0^\ell YI\frac{\partial^2 w}{\partial x^2}\frac{d^2\phi}{dx^2}\,dx + \int_0^\ell cI\frac{\partial^3 w}{\partial x^2\partial t}\frac{d^2\phi}{dx^2}\,dx \\ = k_1[P(E(t)) - P_R]\int_{x_1}^{x_2}\frac{d^2\phi}{dx^2}\,dx\end{aligned} \tag{16}$$

which must hold for all $\phi \in H_0^2(0,\ell)$

The solutions to (16) are approximated using the techniques detailed in Chapter 8 of [19]. Specifically, we consider approximate solutions of the form

$$w^N(t,x) = \sum_{j=1}^{N+1} w_j(t)\phi_j(x)$$

where $\phi_j(x)$ are cubic B-splines modified to satisfy the essential boundary condition at $x = 0$. Use of the basis functions as test functions yields the semi-discrete system

$$\mathbb{M}\ddot{\mathbf{w}} + \mathbb{Q}\dot{\mathbf{w}} + \mathbb{K}\mathbf{w} = k_1[P(E(t) - P_R]\mathbf{b} \tag{17}$$

where

$$\mathbf{w}(t) = [w_1(t)\,,\,\ldots\,,\,w_{N+1}(t)]^T\,. \tag{18}$$

The mass, damping and stiffness matrices are defined by

$$\begin{aligned}[\mathbb{M}]_{ij} &= \int_0^\ell \rho\phi_i\phi_j dx \\ [\mathbb{Q}]_{ij} &= \int_0^\ell \left[\gamma\phi_i\phi_j + cI\phi_i''\phi_j''\right]dx \\ [\mathbb{K}]_{ij} &= \int_0^\ell YI\phi_i''\phi_j'' dx\end{aligned} \tag{19}$$

whereas the force vector has the components

$$[\mathbf{b}]_i = \int_{x_1}^{x_2}\phi_i'' dx. \tag{20}$$

To formulate a first-order semi-discrete system that facilitates implementation using standard ODE routines, we let $\mathbf{z} = [\mathbf{w}, \dot{\mathbf{w}}]^T$ and define the system matrix $\mathbb{A}$ and the vector $\mathbf{B}$ by

$$\mathbb{A} = \begin{bmatrix} 0 & \mathbb{I} \\ -\mathbb{M}^{-1}\mathbb{K} & -\mathbb{M}^{-1}\mathbb{Q}\end{bmatrix}\quad,\quad \mathbf{B} = \begin{bmatrix} 0 \\ \mathbb{M}^{-1}\mathbf{b}\end{bmatrix}. \tag{21}$$

The second-order system (17) can subsequently be reformulated as

$$\begin{aligned}\dot{\mathbf{z}}(t) &= \mathbb{A}\,\mathbf{z}(t) + k_1[P(E(t)) - P_R]\mathbf{B} \\ \mathbf{z}(0) &= \mathbf{z}_0\end{aligned} \tag{22}$$

where the $2N \times 1$ vector $\mathbf{z}_0$ denotes the projection of the initial conditions into the approximating subspace.

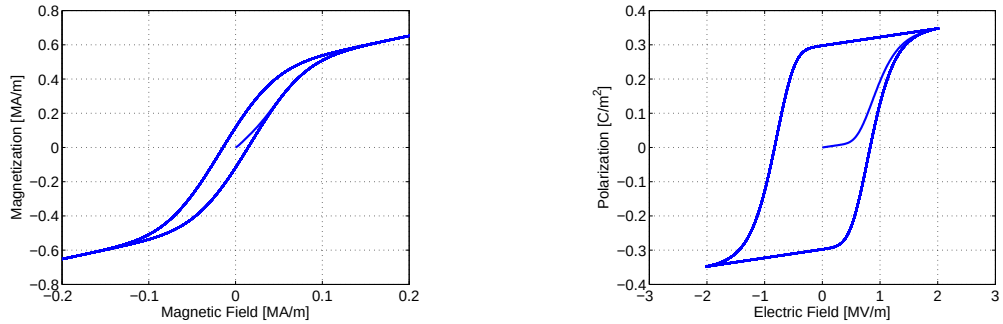

Figure 1. Major hysteresis loop for Terfenol-D (left) and PZT5H (right).

4. Simulation Results

Simulations of the frequency characteristics of one ferromagnetic and one ferroelectric material are presented in this section. The ferromagnetic material Terfenol-D [11] was chosen since it is widely employed and exhibits moderate hysteresis but significant nonlinear effects, while the ferroelectric material PZT5H was chosen to exhibit large hysteresis but relatively less significant nonlinear characteristics. For the ferromagnetic material, Terfenol-D, thermal relaxation was considered. This accounts for rate effect that was found necessary to fit the experimental data of the magnetic actuator [5]. For the ferroelectric material, PZT5H was used and chosen to have negligible thermal relaxation. The HEM model parameters that are representative of these materials are shown in Table 1. The curves represented by these parameters are compiled in Figure 1.

Table 1. Parameter set (P-E or M-H).

	ferromagnetic	ferroelectric
η	$0.9291\frac{\mathrm{m}}{\mathrm{A}}$	$4\cdot 10^7\frac{\mathrm{m}}{\mathrm{A}}$
M_r/P_r	$4.369\cdot 10^5\frac{\mathrm{A}}{\mathrm{m}}$	$0.3\frac{\mathrm{C}}{\mathrm{m}^2}$
$\bar{H}_c/\bar{E}_c$	$1673\frac{\mathrm{A}}{\mathrm{m}}$	$7.6\cdot 10^5\frac{\mathrm{V}}{\mathrm{m}}$
c	$903.5563\frac{\mathrm{A}}{\mathrm{m}}$	$0.237\cdot\frac{\mathrm{V}}{\mathrm{m}}$
b	$4.7729\cdot 10^4\frac{\mathrm{A}}{\mathrm{m}}$	$1.26\cdot 10^5\frac{\mathrm{V}}{\mathrm{m}}$
γ	$0.8324\frac{\mathrm{m}^2}{\mathrm{N}}$	
τ	2.0504s	

To compare the two materials, we define a saturation field E_s or H_s that represents a field at which 95% of the saturation polarization/magnetization P_s/M_s is reached. Different drive levels are chosen around a bias of $0.5E_s$, as represented by equations

$$E(t) = 0.5E_s + 0.5E_s\sin(60\cdot 2\pi\cdot t) \tag{23}$$

$$E(t) = 0.5E_s + 0.25E_s\sin(60\cdot 2\pi\cdot t) \tag{24}$$

$$E(t) = 0.5E_s + 0.125E_s\sin(60\cdot 2\pi\cdot t) \tag{25}$$

for the ferroelectric case. For the analogous ferromagnetic case, the drive levels selected are represented by equations (23-25) with H_s substituted in the place of E_s and $H(t)$ instead of $E(t)$.

The resulting minor loops are shown in Figure 2. Figure 3 shows polarization and magnetization vs. time plots. The frequency response is represented in Figure 4.

For the chosen physical parameter set, Figure 4 demonstrates that the ferromagnetic material exhibits a higher harmonics and, in particular, has a strong second harmonic. The ferroelectric material, despite having a large major loop hysteresis does not exite higher harmonics (Figure 4) and exhibits a nearly linear minor loop behavior (Figure 2). This motivates a further investigation of effects of hysteresis and nonlinearity on material

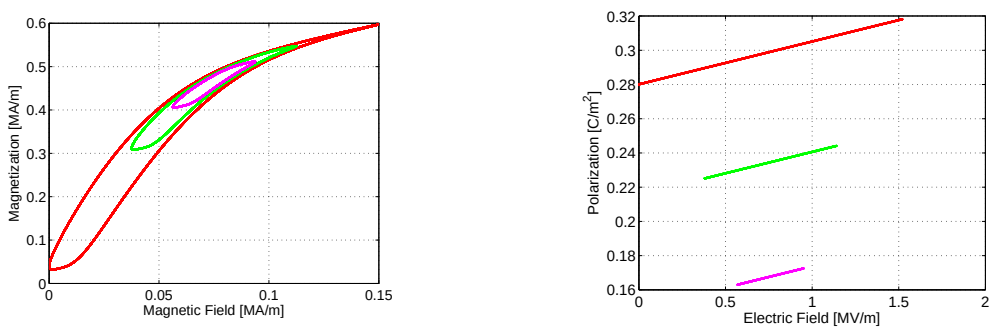

Figure 2. Minor hysteresis loops for Terfenol-D (left) and PZT5H (right).

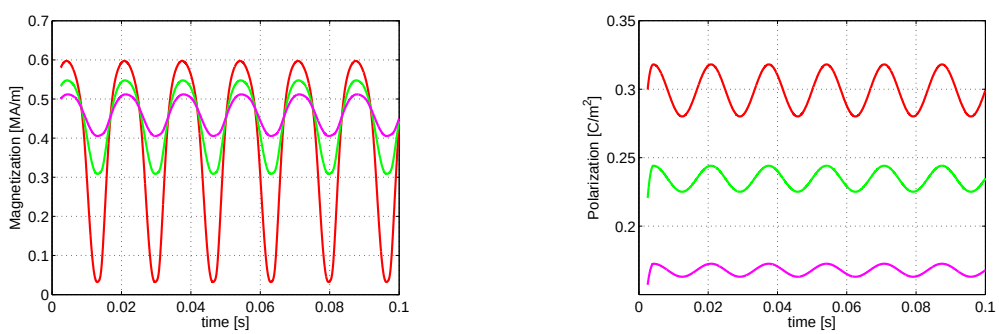

Figure 3. Time domain response for Terfenol-D (left) and PZT5H (right) for inputs (23-25).

Figure 4. Frequency domain response for Terfenol-D (left) and PZT5H (right) for inputs (23-25).

behavior. Since the ferromagnetic material exhibits great higher harmonic content than the ferroelectric for similar drive levels, it was chosen as a baseline to study the sensitivity of frequency response to model parameters.

The model parameters b, c and E_c were systematically varied as these parameters correlate to the following aspects of the nonlinear hysteresis behavior: E_c or mean value of coercive field affects the hysteresis; c (indicative of standard deviation in E_c) affects the slope of the switching region; b (indicative of standard deviation in E_I) affects the potential wells, the nonlinear nature of the material and the degree to which switching occurs prior to the remanence value. Starting with baseline values of the ferromagnetic material, the parametes, b, c and E_c were halved, decreased to 1/4, doubled and quadrupled. The effect of this parameter variation on the parameter space behavior is shown in Figures 5(a)-5(c). Corresponding frequency domain effects are presented in Figures 6(a)-6(c). Finally, an understanding of the AC bias on the nonlinearities was obtained by the driving equations

$$M(t) = 0.25H_s + 0.125H_s \sin(60 \cdot 2\pi \cdot t) \tag{26}$$

$$M(t) = 0.5H_s + 0.125H_s \sin(60 \cdot 2\pi \cdot t) \tag{27}$$

$$M(t) = 0.75H_s + 0.125H_s \sin(60 \cdot 2\pi \cdot t) \tag{28}$$

and is shown in Figures 5(d) and 6(d).

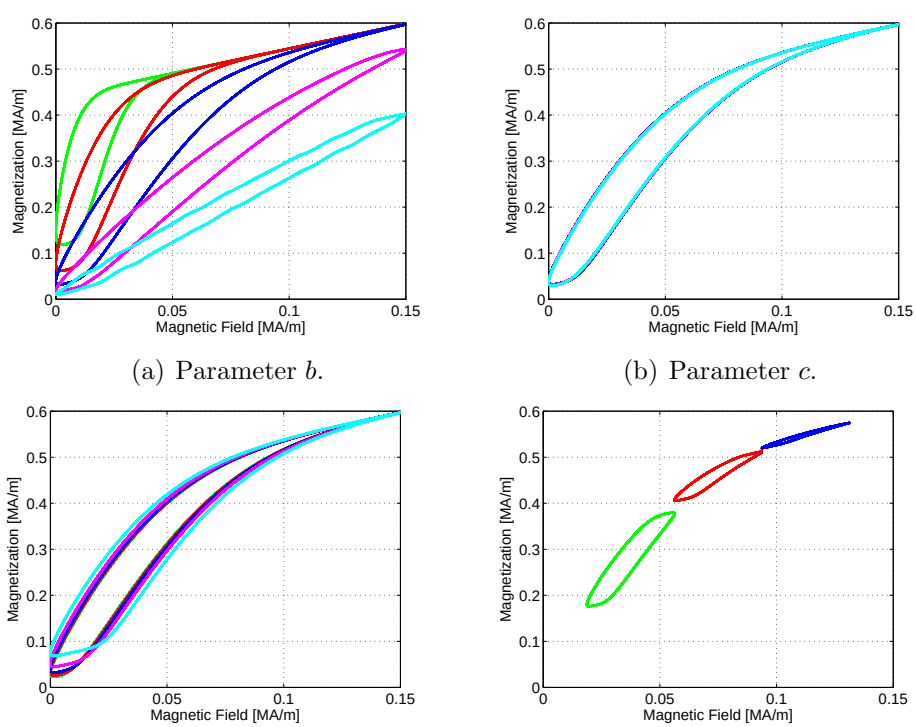

(a) Parameter b.

(b) Parameter c.

(c) Parameter E_c.

(d) Different driving regimes.

Figure 5. Minor loops (a)–(d) for Terfenol-D with different values of b, c, E_c and different driving regimes.

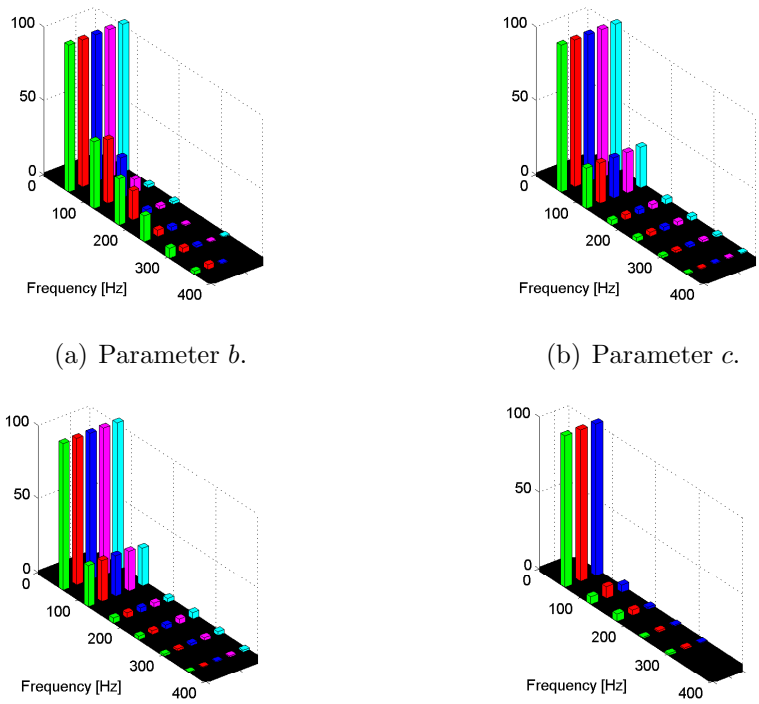

(a) Parameter b.

(b) Parameter c.

(c) Parameter E_c.

(d) Different driving regimes.

Figure 6. FFT (a)–(d) for Terfenol-D with different values of b, c, E_c and different driving regimes.

4.1. Discussion of Results

Whereas the Terfenol-D exhibits relatively smaller major loop hysteresis than PZT5H (Figure 1) for the chosen physical parameter set, it exites significant higher harmonics than PZT5H (Figure 4). This indicates that large major loop hysteresis does not necessarily lead to generation of large higher harmonics particularly when operating in minor loops or restricting the drive field to only positive values. This is further supported by the near-linear behavior of the minor loops PZT5H in contrast to the more nonlinear minor loops in Terfenol-D (Figure 2). Comparing Tables 2 and 3 (normalized FFT coefficients for both materials), we see that at drive fields $0.5H_s \pm 0.5H_s$ (full range of positive field), the second harmonic is nearly 28% of the amplitude of the output at the driving frequency. This decreases to 7.7% (still significant) when the drive amplitude is decreased 1/4th. In contrast, the PZT5H exhibits a maximum of 4.3% amplitude in the second harmonic. Further, the third harmonic and above are not very significant for both materials.

Since, Terfenol-D exhibits a more nonlinear frequency domain behavior, its parameters were used as a baseline for sensitivity study to model parameters. A change in the standard deviation of the interaction field had a considerable effect on the shape of the M-H minor loop curves (Figure 5(a)) and consequently on the second harmonic content as Figure 6(a) shows. Changes in the coercive field mean or distribution produce

Table 2. Normalized FFT values for Terfenol-D.

Input	Harmonic					
	1	2	3	4	5	6
(26)	100.00	27.80	3.36	2.90	1.70	0.74
(27)	100.00	16.51	2.14	1.87	1.26	0.63
(28)	100.00	7.70	3.60	1.21	1.16	0.30

Table 3. Normalized FFT values for PZT5H.

Input	Harmonic					
	1	2	3	4	5	6
(23)	100.00	2.10	1.81	1.49	1.21	1.02
(24)	100.00	3.72	2.99	2.27	1.73	1.41
(25)	100.00	4.29	3.39	2.50	1.85	1.50

almost no modification to the minor loop $M - H$ curves (Figures 5(b) and 5(c)) and consequently to the frequency response (Figures 6(b) and 6(c)). An investigation of the effect of DC bias (Figure 5(d)) reveals that the most nonlinear frequency response (or highest second harmonic content) is observed at $0.5H_s$ or in the middle of the positive range (Figure 6(d)).

5. Experimental Results and Model Correlation of Beam Driven by PZT Patches

To illustrate the effect and quantification of hysteresis effects on frequencies for an experimental device, we consider an aluminum cantilever beam, as modeled in Section 2, 3 and 4, driven by surface-mounted piezoceramic patches. The experimental beam had length $\ell = 0.395$ m, width $b = 0.0265$ m and thickness $h = 0.00103$m. The first fundamental harmonic was at 4.5 Hz. The driving patches had the same width as the beam and covered the region $[x_1, x_2] = [0.045, 0.05]$ m. The beam acceleration was measured using an accelerometer located at $\bar{x} = 0.38$ m. The input voltage and field are related by the equation $E = V/h_p$ where the patch thickness is $h_p = 3.05 \times 10^{-4}$ m.

To demonstrate the effect of the coupling between the cantilever structure and the nonlinear response of the ferroelectric material, two scenarios are considered. In the first case, an input driving frequency of 2.25 Hz, which is half the value of the resonance frequency of the structure, is used. The expectation is that the second harmonic (4.5 Hz) produced due to the nonlinear response of the piezoelectric material

is selectively amplified by the cantilever structure as it coincides with its resonance frequency. Therefore, the second harmonic is expected to have a strong presence in the vibrations of the cantilever beam. In the second case, the system is driven at 3 Hz, so the second harmonic does not coincide with the resonance frequency. Hence, the second harmonic content in the cantilever vibration is likely to be weak when driven at this frequency.

It can be observed in Figure 8 that both the experimental data and model simulation show the presence of a strong second harmonic as was expected. To compare the various harmonics the amplitude at the drive frequency was normalized to 100 and all other amplitudes were scaled accordingly. Thus, relative to the amplitude of the response at the driving frequency, the amplitude of the second harmonic is 40% (simulation) and around 30% (experiment) while the third and fourth harmonics are respectively around 10% and 5%.

The analysis of this second harmonic illustrates some interesting physics. For example, the second harmonics in Table 4.1 show that even at extremely high drive amplitudes compared to those used in this experiment, the amplitude of the second harmonic generated by just the PZT material is less than 5% of the amplitude of the first harmonic. This shows that a linear system such as a cantilever beam coupled to a weakly nonlinear piezoelectric material can produce a strong harmonic distortion. This nonlinearity can also be seen in the time domain data in Figure 7 as the waveforms deviate from a pure sinusoid. Finally, the parameter space plots in Figure 9 shows the model fit is not as nonlinear as the experimental data though the hysterisis is modeled well. This possibly explains why the model under-predicts the amplitude of the second harmonic relative to the experimental data in Figure 8.

In the case of driving frequency of 3 Hz, the second harmonic at 6 Hz generated by the piezoceramic patch is not significantly amplified by the structure as it does not coincide with its harmonic peak. Hence, relative to the response at the drive frequency, its amplitude is around 5-6% as shown in Figure 8. Hence, the time domain response also does not show significant devaitions form pure sinusoidal behavior as can be observed in Figure 7. The parameter space plots in Figure 9 show good model fit to the experimental data.

Overall, the model characterizes both the hysteretic and nonlinear relation between the voltage and acceleration as well as the time and frequency behavior of the acceleration within reasonable error limits. This error is likely to be minimized by further improvements in estimation of model parameters. Hence, it provides a framework for quantifying the fundamental frequency behavior of the material in a manner that facilitates subsequent inversion for linear control design.

6. Conclusions

This investigation shows that significant (about 28%) second harmonic behavior can be produced when these materials are driven at high amplitudes. It appears that higher

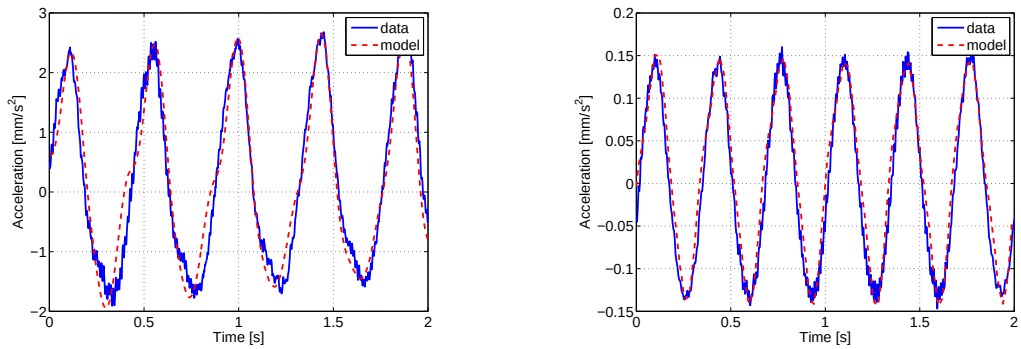

Figure 7. Time domain response for 2.25 Hz (left) and 3 Hz (right) input.

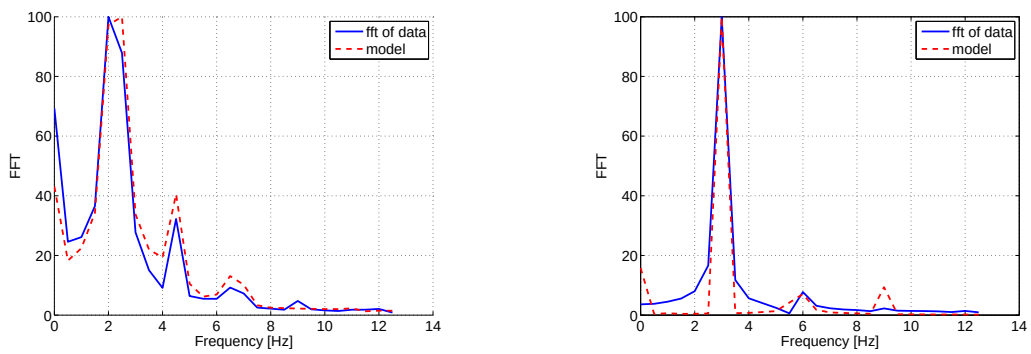

Figure 8. Frequency domain response for 2.25 Hz (left) and 3 Hz (right) input.

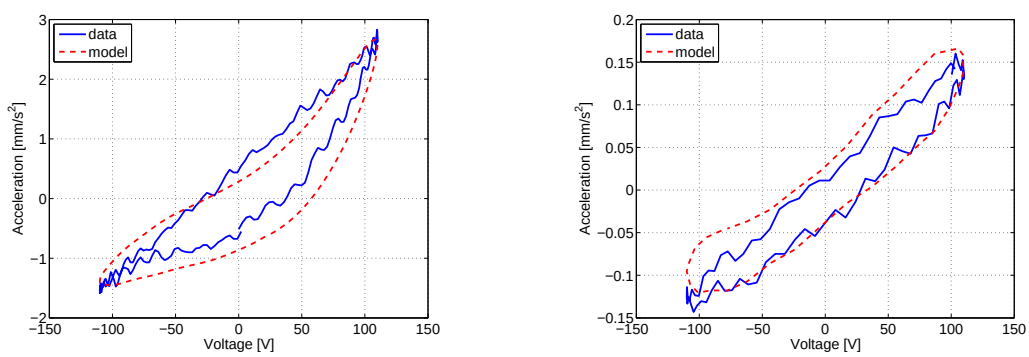

Figure 9. Hysteresis curve for 2.25 Hz (left) and 3 Hz (right) input.

harmonics produced for minor loop excitations are strong functions of nonlinearity (quantified by distribution of interactive field in Homogenized Energy Model), drive amplitude and DC bias field applied. Major loop hysteresis (and Homogenized Energy Model parameters for mean and standard deviation of coercive field) produce almost no change in higher harmonic content. A more detailed study with several materials and experimental frequency domain data may prove useful in confirming these trends.

This study shows that a linear system such as a cantilever beam coupled to a weakly nonlinear piezoelectric material can produce a strong harmonic distortion. The Homogenized Energy Model has the framework to quantify this behavior making it a useful inversion tool for linear control design.

Acknowledgments

The research of MS was supported through the NSF Grant DMS-0636590, EMSW21-RTG program while the research of JA was supported in part by the Office of Naval Research through the subcontract 05C0165-Sub 7. The research of RCS was supported in part by the Air Force Office of Scientific Research through the grants AFOSR-FA9550-04-1-0203 and AFOSR-FA9550-08-1-0348. The authors thank Adam Attarian, Grace Kepler and Hien Tran (NCSU) for their assistance in collecting the experimental beam data.

References

[1] W.D. Armstrong, "Magnetization and magnetostriction processes in Tb-(0.27-0.30)Dy-(0.73-0.70)Fe-(1.9-2.0)", *J. Appl. Phys.*, Volume 81, pp. 2321–2326, 1997.

[2] W.D. Armstrong, "An incremental theory of magneto-elastic hysteresis in pseudo-cubic ferro-magneto-strictive alloys", *J. Magn. Magn. Mater.*, Volume 263, pp. 208–218, 2003.

[3] J. Atulasimha, G. Akhras and A.B. Flatau, "Comprehensive three dimensional hysteretic magneto-mechanical model and its validation with experimental single-crystal iron-gallium behavior", *Proceedings of the 52nd Annual Conference on Magnetism and Magnetic Materials*, 103(7), 2007.

[4] T.R. Braun and R.C. Smith, "High Speed Model Implementation and Inversion Techniques for Ferroelectric and Ferromagnetic Transducers", *J. of Intelligent Material Systems and Structures*, 19(11), pp. 1295–1310, 2008.

[5] T.R. Braun, R.C. Smith and M.J. Dapino, "Experimental validation of a homogenized energy model for magnetic after-effects", *Applied Physics Letters*, 88(12), 2006.

[6] D. Capecchi, R. Masiani and F. Vestroni, "Periodic and Non-Periodic Oscillations of a Class of Hysteretic Two degrees of Freedom Systems", *Nonlinear Dynamics*, Volume 13, pp. 309–325, 1997.

[7] C. Christopoulos, "Frequency Response of Flag-Shaped Single Degree-of-Freedom Hysteretic Systems", *Journal of Engineering Mechanics*, Volume 8, pp. 894–903, 2004.

[8] M.J. Dapino, "Magnetostrictive materials," *Encyclopedia of Smart Materials*, M. Schwartz, Ed., John Wiley and Sons, New York, pp. 600–620, 2002.

[9] M.J. Dapino, F.T. Calkins and A.B. Flatau, "Magnetostrictive devices," *Wiley Encyclopedia of Electrical and Electronics Engineering*, John G. Webster, Ed., John Wiley and Sons, Inc., New York, Volume 12, pp. 278–305, 1999.

[10] E. Della Torre, *Magnetic Hysteresis*, IEEE Press, New York, 1999.

[11] Etrema Products, Inc, `http://www.etrema-usa.com`

[12] P.G. Evans and M.J. Dapino, "State-Space Constitutive Model for Magnetization and Magnetostriction of Galfenol Alloys", *IEEE Transactions on Magnetics*, 44(7), 2008.

[13] R.V. Iyer and X. Tan, "Control of hysteretic systems through inverse compensation," *IEEE Control Systems Magazine*, 29(1), pp. 83–99.

[14] D.C. Jiles and D. L. Atherton, "Theory of the Magnetization Process in Ferromagnets and its Application to the Magnetomechanical Effect", *Journal of Physics D: Applied Physics*, 17(6), pp.1265-1281, 1984.

[15] J.A. Main and E. Garcia, "Piezoelectric stack actuators and control system design: strategies and pitfalls," *Journal of Guidance, Control, and Dynamics.* 20(3), pp. 479–485, 1997.

[16] J.A. Main, E. Garcia and D.V. Newton, "Precision position control of piezoelectric actuators using charge feedback," *Journal of Guidance, Control, and Dynamics.* 18(5), pp. 1068–73, 1995.

[17] I.D. Mayergoyz, *Mathematical Models of Hysteresis,* Springer–Verlag, New York, 1991.

[18] J.B. Restorff, "Magnetostrictive materials and devices," *Encyclopedia of Applied Physics*, Volume 9, pp. 229–244, 1994.

[19] R.C. Smith, *Smart Material Systems – Model Development*, SIAM, Philadelphia, 2005.

[20] R.C. Smith, A.G. Hatch, T. De, M.V. Salapaka, R.C.H. del Rosario and J.K. Raye, "Model Development for Atomic Force Microscope Stage Mechanisms", *SIAM J. of Appl. Math.*, 66(6), 1998–2026, 2006.

[21] R.C. Smith, S. Seelecke, M. Dapino and Z. Ounaies, "A unified framework for modeling hysteresis in ferroic materials", *Journal of the Mechanics and Physics of Solids*, 54(1), pp. 46–85, 2006.

[22] X. Tan and J.S. Baras, "Modeling and control of hysteresis in magnetostrictive actuators," *Automatica*, 40(9), pp. 1469–1480, 2004.

[23] X. Tan and O. Bennani, "Fast inverse compensation of Preisach-type hysteresis operators using field-programmable get arrays," Proceedings of the American Control Conference, Seattle, WA, pp. 2365–2370, 2008.

[24] X. Tan, R. Venkataraman and P.S. Krishnaprasad, "Control of hysteresis: Theory and experimental results," Smart Structures and Materials 2001, Proceedings of the SPIE, Volume 4326, pp. 101–112, 2001.

[25] K. Uchino, *Piezoelectric Actuators and Ultrasonic Motors*, Kluwer Academic Publishers, Boston, 1997.

[26] J.H. Zhang, "Spectral Analysis For Systems With Hysteretic Restoring Force", *Mechanical Systems and Signal Processing*, 10(1), pp. 19–28, 1996.